ACS OMEGA

http://pubs.acs.org/journal/acsodf

Article

Optimization and Uncertainty Quantification Method for Reservoir Stimulation through Carbonate Acidizing

Qasim Sahu, Marwan Fahs, and Hussein Hoteit*

Cite This: *ACS Omega* 2023, 8, 539−554

Read Online

ACCESS | Metrics & More | Article Recommendations

ABSTRACT: Reservoir stimulation is a widely used technique in the oil and gas industry for increasing the productivity of hydrocarbon reservoirs, most notably in carbonate formations. This work aims to develop an optimization workflow under uncertainty for matrix acidizing. A reactive transport model is implemented in a finite-element framework to simulate the initiation and propagation of dissolution channels in porous carbonate rock. The model is verified using an analytical solution. We utilize surrogate modeling based on polynomial chaos expansion (PCE) and Sobol indices to identify the most significant parameters. We investigate the effect of varying 12 identified parameters on the efficiency of the stimulation process using dimensionless groups, including the Damköhler, Peclet, and acid capacity numbers. Furthermore, the surrogate model reproduces the physics-based results accurately, including the dissolution channels, the pore volume to breakthrough, and the effective permeability of the stimulated rock. The developed workflow assesses how uncertainties propagate to the model's response, where the surrogate model is used to calculate the univariate effect. The global sensitivity analysis shows that the acid capacity number is the most significant parameter for the pore volume to breakthrough with the highest Sobol index. The marginal effect calculated for the individual parameter confirms the results from Sobol indices. This work provides a systematic workflow for uncertainty analysis and optimization applied to the processes of rock stimulation. Characterizing the impact of uncertainty provides physical insights and a better understanding of the matrix acidizing process.

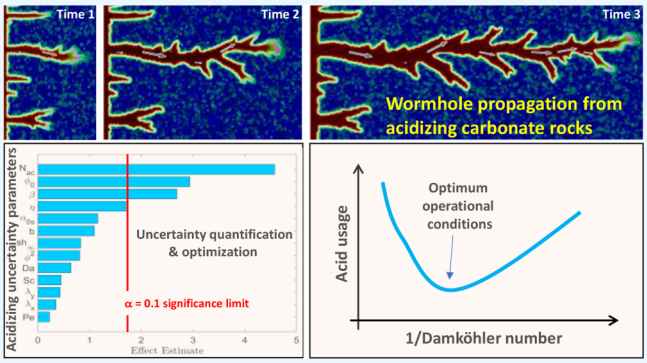

1. INTRODUCTION

Substantial proportions of hydrocarbon fuels reside in carbonate reservoirs. Several studies estimated that more than 60% of the world's oil reserves are trapped in carbonate reservoirs.[1−3] However, several challenges hinder efficient recovery from these reservoirs, such as rock heterogeneity at different length scales, drilling-induced damage, and tight formation. Damage to the reservoir from various operations causes plugging of the pores and decreases the effective permeability near the wellbore region, leading to flow restriction and poor well productivity.[4] Well stimulation is a popular method used to improve productivity from carbonate reservoirs, where the near-wellbore flow transmissibility is enhanced by injecting different chemicals into the reservoir.[5] The success of the operation needs to optimize the used volume of chemicals (i.e., the cost) and the incremental deliverability of the well.

Matrix acidizing in carbonates is an effective stimulation method to increase productivity.[6] Its treatment typically involves injecting a reactive chemical into the porous medium at a pressure below the rock's fracturing pressure. The reactive fluid tends to dissolve the rock minerals, creating high-conductive pathways (wormholes) for the flow of subsurface fluids. The choice of the reactive fluid strongly depends on the formation mineralogy and the subsurface pressure and temperature conditions. For example, in carbonate rocks, where the dominant minerals are calcite and dolomite, hydrochloric, emulsified, citric, acetic, and chelating acids are the typical solutions used in the treatment.[7−13] The initiation and propagation of the induced wormholes depend on many parameters, including the relative magnitude of the rate of acid transport to the rate of reaction, temperature, mineralogy, and porous medium properties at different length scales.[14−16]

Extensive work has been conducted in the literature to understand wormhole initiation and propagation in carbonate rocks (WIPCR). Experimental work in the core flooding setup was first conducted to understand the parameters that control the acidizing in carbonate rocks. These experimental studies analyzed the impact of rock properties, injection conditions,

Received: August 29, 2022
Accepted: November 29, 2022
Published: December 22, 2022

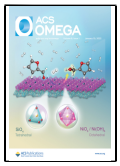

pressure, mineralogy, temperature, and reaction kinetics on the created channels.[17−21] In those linear core flooding experimental studies, the acidic solution is injected at a different rate in a cylindrical core sample, and the pore volume to the breakthrough was measured along with the other pressure measurements.[20,22,23]

Different modeling approaches have been developed to study the governing multiphysical processes to simulate and validate the results of laboratory experiments and to optimize the design of field deployment. These approaches can be summarized into three categories.[24] The first one is the capillary tube approach,[25] which uses cylindrical tubes to represent wormholes, assuming that their shape and location are predetermined. The model enables studying the effect of reaction kinetic and fluid transport on the wormhole penetration rate but cannot predict wormhole initiation as it assumes a preexisting channel. The second approach is based on a network model to mimic rock dissolution. In this model, the porous medium is represented by interconnected tubes, where the Hagen−Poiseuille equation is used to capture the flow of the acidic solution.[26,27] Currently, the network model, also known as the pore-scale model, is built from high-resolution scanning techniques, where the flow processes are simulated at the pore scale.[22,28,29] As a result, this approach exhibits limitations related to the required computational resources and implementation at the field scale. The third approach is a continuum-based or averaged-based model that couples fluid flow, species transport, and fluid/rock reaction, including the dissolution mechanism and induced channel propagation. The flow is assumed to be governed by Darcy's law. A simplified pore-scale concept is utilized to correlate the parameters at the pore scale, such as the pore radius, surface area, and local mass transfer to Darcy-scale parameters.[30−32] The continuum-based model has been extended to consider radial and three-dimensional systems.[33−35] Simulation results showed good agreement with the experimental observation regarding the dissolution pattern and the prediction of pore volume to breakthrough.[36] Other studies expanded the model to consider the influence of temperature,[37] discrete fractures,[38,39] and the presence of a second fluid phase.[40] However, the main limitations of the continuum model are related to the uncertainties of the underlying variables, corresponding to the nature of rock heterogeneity. Quantifying such uncertainties and their impact on the model predictions is of significant interest in optimizing this technology.

This study is based on the continuum model, which involves several parameters related to the rock properties (i.e., pore radius, surface area, and fluid/rock interaction), acid reactivity, and injection conditions. These parameters are often subject to uncertainties, which propagate through the model, leading to variability in the predictions. Thus, it is vital to develop a workflow to quantify how uncertainties in the model inputs propagate to the model's output. We propose an uncertainty propagation analysis, which, to the best of our knowledge, has never been performed for WIPCR. Existing approaches in the literature examined the sensitivity of the underlying parameters such as rock properties, reaction rate, diffusion coefficient, and pore-scale parameters using one variable at a time, which is inefficient and does not capture parameter dependencies.[30,33,41] Alternatively, a more general and robust framework of uncertainty propagation is the global sensitivity analysis (GSA). GSA can provide more insights into this problem by considering the dependencies among parameters. This feature is important for applications that involve strong coupling between different physical processes, such as WIPCR. In other fields, many studies utilized this approach to examine complex problems in the subsurface, such as studying carbon dioxide storage,[42] reservoir simulation,[43−45] reactive transport,[46,47] and natural convection in porous media.[48−51] For instance, Benetatos and Giglio introduced a comprehensive workflow for full-scale reservoir simulation, including multiple data sources.[52] However, GSA has not yet been applied to WIPCR. The goal of this work is to develop a GSA method for WIPCR, which allows improving uncertainty quantification and optimization of the carbonate dissolution processes.

A dimensionless analysis is developed to perform the GSA. We consider the impact of uncertainties on the model dimensionless parameters, including the convection Damköhler number, the diffusion Damköhler number, the Peclet number, the acid capacity number, pore volume injection to breakthrough, and the effective permeability of the system. WIPCR modeling requires a large number of forward simulations, which involve nonlinear coupling between multiphysical processes. Moreover, the number of input parameters is relatively large. To mitigate this challenge, we present a new strategy based on coupling a variance decomposition technique and a screening method. We used the screening method to identify the most significant variables to reduce the model's dimensions. The variance decomposition technique is then used to rank the most important parameters based on the contribution of every parameter to the selected model's output.[53] The traditional method of calculating these sensitivity indices uses Monte Carlo simulations, which is impractical to use with expensive computational models. To overcome this issue, we utilize polynomial chaos expansion (PCE)[54,55] as a surrogate for the full-physics model. Once the PCE is built, further processing of the coefficients in the PCE allows the calculation of the sensitivity indices.

This paper is organized as follows: Section 2 presents the mathematical model and the nondimensional analysis. Section 3 is devoted to the methodology, where we present the numerical model and the global sensitivity method. In Section 4, we validate the numerical model against an analytical solution for carbonate dissolution. Section 5 presents the results and discussion of the GSA, followed by the main conclusion in Section 6.

2. PROBLEM DESCRIPTION

Wormhole formation and dissolution is a process that occurs at different length scales of the porous medium. The reactive fluid propagates within the rock pore and exhibits a wide range of pore distributions in shape and size. The pores are enlarged due to rock dissolution at the pore walls, leading to the initiation and propagation of the dissolution channel. Here, we consider a continuum reactive transport model to simulate carbonate acidizing in a rectangular domain. This model considers the dissolution of porous carbonate rocks by acidic solutions at Darcy's scale.[30] The model captures wormhole formation and propagation by correlating the pore radius and the solid−fluid interfacial area to Darcy-scale properties. This coupling is achieved through a structure−property relationship. The model consists of the continuity equation and Darcy's law, which are used to obtain the pressure field, such that,

$$\mathbf{U} = -\frac{1}{\mu}\mathbf{K}\cdot\nabla P \tag{1}$$

https://doi.org/10.1021/acsomega.2c05564
ACS Omega 2023, 8, 539−554

$$\frac{\partial \varphi}{\partial t} + \nabla \cdot \mathbf{U} = 0 \tag{2}$$

where $\mathbf{U}$ is the flow velocity vector [m/s], $\mathbf{K}$ is the absolute permeability [m^2], P is the pressure [Pa], μ is the viscosity [Pa·s] of the solution, and φ is the porosity [−].

The species balance equation, given by a convection−diffusion−reaction equation, is given by

$$\frac{\partial(\varphi C_f)}{\partial t} + \nabla \cdot (\mathbf{U} C_f) = \nabla \cdot (\varphi \mathbf{D_e} \cdot \nabla C_f) - k_c a_v (C_f - C_s) \tag{3}$$

$$C_s = \frac{C_f}{\left(1 + \frac{k_s}{k_c}\right)} \tag{4}$$

where C_f is the acid concentration [mol/m^3], $\mathbf{D_e}$ is the effective dispersion−diffusion tensor [m^2/s], k_c is the local mass transfer coefficient [m/s], a_v is the solid−fluid interfacial area [1/m], C_s is the concentration of the acid at the fluid−solid interface [mol/m^3], and k_s is the surface reaction rate [m/s]. Acidizing carbonate causes the dissolution of the rock mineral. This dissolution is captured at Darcy's scale by a change in porosity as follows:

$$\frac{\partial \varphi}{\partial t} = \frac{k_c (C_f - C_s) a_v \alpha}{\rho_s} \tag{5}$$

where α is the acid dissolving power, defined as the mass of minerals consumed by a given mass of acid [kg/mol], and ρ_s is the density of the carbonate rocks [kg/m^3]. Eq 3 describes the acid species transport at Darcy's scale. The last term in this equation represents the transport of the acid from the bulk fluid phase to the solid−fluid interface. One assumption is that the dissolution does not affect the density and viscosity of the fluid. The mathematical model is completed by relating the pore radius and solid−fluid interfacial area to the change in local porosity, permeability, and mass transfer coefficient, as described below.

As the acid dissolves the rock, the porous medium structure changes at different length scales. At Darcy's scale, the rock permeability and porosity are altered, while at the pore scale, the pore radius, the interfacial area, and pore connectivity are continuously varying. Different correlations have been empirically formulated to relate these properties.[56] In this study, we consider a modified Carman−Kozeny correlation to relate the increase in porosity to the permeability as a result of dissolution, that is,

$$\frac{k}{k_0} = \left(\frac{\varphi}{\varphi_0}\right)\left[\frac{\varphi(1-\varphi_0)}{\varphi_0(1-\varphi)}\right]^{2\beta} \tag{6}$$

where k is the current permeability [m^2], k_0 is the initial permeability [m^2], φ_0 is the initial mean porosity [−], and β is a constant [−]. The following relationships capture the variation in the pore radius and surface area available for the reaction:

$$\frac{r_p}{r_{p0}} = \sqrt{\frac{k\varphi_0}{k_0\varphi}}, \frac{a}{a_{v0}} = \frac{\varphi r_0}{\varphi_0 r_p}\frac{r_p}{r_{p0}} = \sqrt{\frac{k\varphi_0}{k_0\varphi}}, \frac{a_v}{a_{v0}} = \frac{\varphi r_{p0}}{\varphi_0 r_p} \tag{7}$$

Here, r_p represents the relative change of the pore radius [m], r_{p0} is the initial relative change of the pore radius, and a_{v0} is the initial interfacial area [1/m]. The mass transfer coefficient (k_c) is calculated with the following relationship:[57,58]

$$Sh = \frac{2k_c r_p}{D_m} = Sh_\infty + bRe_p^{1/2}Sc^{1/3} \tag{8}$$

where Sh is the dimensionless Sherwood number [−], D_m is the acid molecular diffusion coefficient [m^2/s], Sh_∞ is the asymptotic Sherwood number [−], b is the local mass transfer constant, Re_p is the Reynolds number at the pore scale [−], and Sc is the Schmidt number [−]. The Reynolds number at the pore scale is defined as follows:

$$Re_p = \frac{2|\mathbf{U}|r_p}{\nu} \tag{9}$$

where ν is the kinematic viscosity [m^2/s]. The Schmidt number is defined by:

$$Sc = \frac{\nu}{D_m} \tag{10}$$

The effective dispersion coefficients are calculated as follows:

$$D_{e,X} = \alpha_{os} D_m + \frac{2\lambda_X \|\mathbf{U}\| r_p}{\varphi}, D_{e,T} = \alpha_{os} D_m + \frac{2\lambda_T \|\mathbf{U}\| r_p}{\varphi} \tag{11}$$

In the above equation, D_{eT} and D_{eX} are the transverse and longitudinal dispersion coefficients [m^2/s], respectively, and λ_x and λ_y are constants that depend on the pore structure [−], and α_{0s} is the pore-connectivity constant [−]. The simulated domain is shown in Figure 1, which represents a commonly used

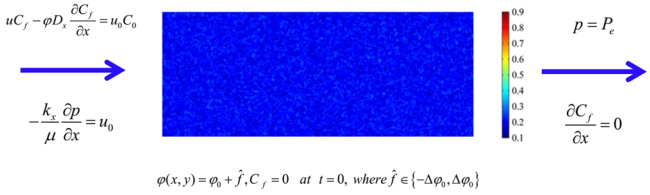

Figure 1. Illustration of the 2D geometry of the simulation domain with initial and boundary conditions; the color map depicts the initial porosity distribution.

benchmark in the literature, mimicking the conditions for a core flooding experiment.[31,40,59] The Danckwert's inflow condition is imposed at the inlet (left side), while Dirichlet boundary conditions (constant pressure) are imposed at the outlet (right side) with no flow at the transverse boundary. The acidic solution is injected through the left side at a constant injection concentration. Outlet boundary conditions (zero dispersive flux) are imposed on the right side. The boundary conditions, along with the geometry, are illustrated in Figure 1.

The initial and boundary conditions are given by

$$uC_f - \varphi D_x \frac{\partial C_f}{\partial x} = u_0 C_0, \quad x = 0 \tag{12}$$

$$-\frac{k_x}{\mu}\frac{\partial p}{\partial x} = u_0, \quad \frac{\partial p}{\partial y} = 0, \quad x = 0 \tag{13}$$

$$n \cdot \nabla p = 0, \quad n \cdot \nabla C_f = 0, \text{ transverse boundries} \tag{14}$$

$$p = p_e, \quad \frac{\partial C_f}{\partial x} = 0, \quad x = L \tag{15}$$

https://doi.org/10.1021/acsomega.2c05564
ACS Omega 2023, 8, 539−554

$$\varphi = \varphi_0 + \hat{f},\ C_f = 0 \quad \text{at } t = 0, \text{ where } \hat{f} \in \{-\Delta\varphi_0, \Delta\varphi_0\} \tag{16}$$

where u_0 is the inlet velocity of the injected solution [m/s], C_0 is the inlet concentration of the acidic solution [mol/m^3], p_e is the pressure at the outlet [Pa], n is a normal vector on the transverse boundary [−], L is the domain length in the flow direction [m], and $\hat{f}$ is a perturbation that is introduced to the initial mean porosity [−] that is varied within the interval [$-\Delta\varphi_0, \Delta\varphi_0$], as shown in Figure 1. This variability is used to introduce bios in the system to determine the initiation of wormholes.

3. DIMENSIONLESS ANALYSIS

The processes of wormhole formation and dissolution are governed by 16 physical parameters: fluid viscosity (μ), fluid kinematic viscosity (ν), surface reaction rate (k_s), acid dissolving power (α), density of the carbonate rocks (ρ_s), initial average permeability (k_0), initial mean porosity (φ_0), the constant of the permeability−porosity relationship (β), initial relative change of the pore radius (r_{p0}), interfacial surface area (a_{v0}), acid molecular diffusion coefficient (D_m), pore-connectivity constant (α_{0s}), dispersion tensor constants (λ_x and λ_y), inlet velocity of the acidic solution (u_0), inlet concentration of the acidic solution (C_0), pressure at the outlet (p_e), perturbation introduced to the initial mean porosity ($\hat{f}$), porosity interval ($\Delta\varphi_0$), and the constant of the local mass transfer equation (b).

In this study, the sensitivity analysis is performed using the dimensionless form of the governing equations. This approach is crucial to extend the results and interpretations of physical processes to multiscale scenarios. The governing equations are expressed in the dimensionless form by introducing the following dimensionless variables:

$$x_D = \frac{x}{L},\ y_D = \frac{y}{L},\ z_D = \frac{z}{L},\ \mathbf{u_D} = \frac{\mathbf{u}}{u_0},\ t_D = \frac{t}{(L/u_0)}$$
$$r_D = \frac{r_p}{r_{p0}},\ A_{vD} = \frac{a_v}{a_{v0}},\ \boldsymbol{\kappa_D} = \frac{\mathbf{k}}{k_0}$$
$$c_{fD} = \frac{C_f}{C_0},\ c_{sD} = \frac{C_s}{C_0},\ p_D = \frac{p - p_e}{\frac{\mu u_0 L}{k_0}} \tag{17}$$

A complimentary list of dimensionless numbers is identified by

$$Da = \frac{k_s a_0 L}{u_0},\quad \phi^2 = \frac{2k_s r_0}{D_m},\quad N_{ac} = \frac{\alpha C_0}{\rho_s},\quad \eta = \frac{2r_0}{L},\quad Pe = \frac{u_0 L}{D_m} \tag{18}$$

where Da is the convection Damköhler number which represents the ratio of reaction rate to convection rate, ϕ^2 is the diffusion Damköhler number which represents the ratio of reaction rate to diffusion rate, N_{ac} is the acid capacity number that reflects the volume of carbonate dissolved in a unit volume of the acid, η is the ratio of the pore-scale to Darcy scale, Pe is the Peclet number which represents the convection rate to diffusion rate. The governing equations in the dimensionless form are provided in Appendix A.

4. METHODOLOGY: NUMERICAL MODEL AND GSA

4.1. Finite-Element Numerical Model. A finite-element model is developed, using COMSOL multiphysics, to solve the system of nondimensional equations. The momentum equation is defined in the porous medium flow module, where the pressure and flow velocity are calculated. The convection−diffusion−reaction equation is defined by the transport of diluted species in porous media under the chemical species transport module. Furthermore, we use the domain ordinary-differential equation to define the mass conservation equation where the porosity change with time is captured. We utilize local variables to define the structure−property relationships. This step updates the permeability, pore radius, interfacial surface area, and local mass transfer coefficient. We select second-order discretization for the shape function in the species transport equation, the mass conservation equation, and linear elements discretization for the momentum equation. For solver configuration, we use a segregated solver approach where the set of equations is solved sequentially. Multifrontal massively parallel sparse direct solver (MUMPS) is used to solve the resulting system of equations.

4.2. GSA Workflow. GSA is used to perform uncertainty propagation analysis aiming at understanding how the variability in the reactive transport model is impacted by the variability of inputs. This process is essential in subsurface applications with uncertainties in the rock and fluid-rock properties. For instance, important properties used in modeling carbonate dissolution are the distribution of the pore radius and interfacial surface area, which can vary by several orders of magnitude. The processes of WIPCR are governed by 20 physical parameters. With the dimensional analysis, we could regroup these parameters into 13 dimensionless parameters with uncertainties. GSA allows ranking the dimensionless input parameters according to their significance to the objective function. The variance decomposition technique[60] has several advantages; it has been widely used in applications related to coupled flow and transport in porous media.[49,61,62] However, for WIPCR, even with the 1D analysis, the number of input parameters is still large. Thus, the variance decomposition technique is impractical as it requires many runs of the forward model.

To overcome this challenge, we present a robust strategy for WIPCR modeling that allows reducing computational requirements and the number of assessed parameters. The analysis follows a black-box approach, which is based on the model's response to a given distribution of the model's inputs. The GSA workflow consists of multiple steps, including parameter screening, design of experiments (DoE), variance decomposition, and Sobol indices (SI), as detailed below.

4.2.1. Parameter Screening and DoE. This step aims to identify the significant parameters in the model based on a screening analysis performed using a simplified DoE. Reducing the dimensions of the model allows performing a detailed GSA with the variance decomposition method. The screening method uses DoE to maximize the information about the model response and structure with reduced computational time.

In our study, we used the folded Plackett−Burman design as a screening method.[63,64] This DoE uses runs that are a multiple of four that provides an efficient evaluation of the response in the objective function with a reasonable number of simulations. Based on the screening method, several insignificant parameters can be disregarded in the sensitivity analysis. The sensitivity of the remaining significant parameters requires a more accurate

https://doi.org/10.1021/acsomega.2c05564
ACS Omega 2023, 8, 539−554

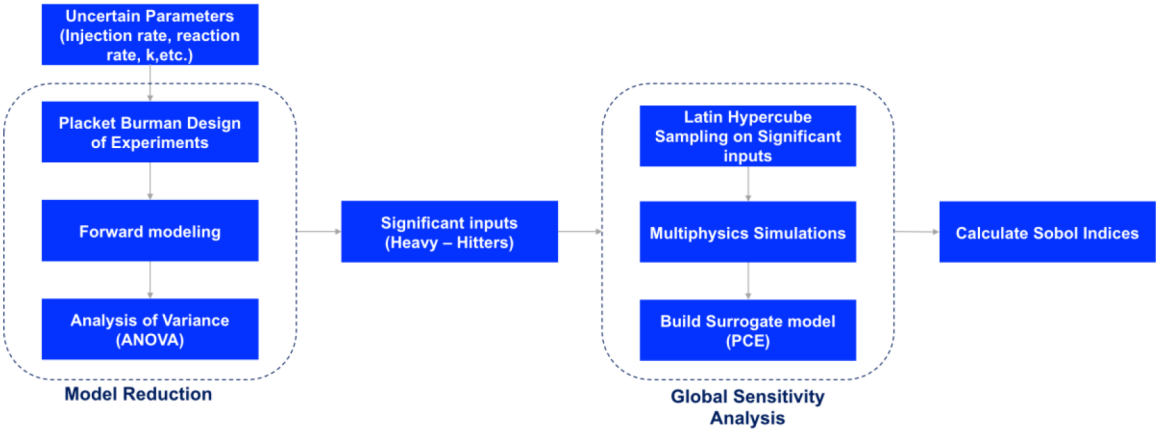

Figure 2. Workflow of the proposed GSA.

technique to capture dependencies among the model parameters.

4.2.2. Variance-Based Technique: Sobol Indices. One of the most effective methods in sensitivity analysis is the variance-based technique, where Sobol indices (Sis) are used as sensitivity matrices.[49,54] This approach does not require linearity in the physical model and can be used to study complex models. The traditional approach to computing Sobol indices is through Monte Carlo simulations, which requires a large set of experimental designs that make it impractical. To overcome this problem, we use PCE as a surrogate model for the simulation model to calculate the Sobol sensitivity indices and the marginal effect. The GSA workflow with different computational steps is illustrated in Figure 2. Additional details are provided in Appendix B.

4.3. Verification of the Numerical Model. This section aims to investigate the correctness of the numerical model, which is a prerequisite step before GSA analysis. We verify the simulation model with a 1D analytical solution. Simulations were performed on the domain shown in Figure 1, mimicking core flooding acidizing experiments. The input parameters are specified in subsequent sections.

4.3.1. Verification with 1D Analytical Solution. The multiphysical processes of WIPCR are not intrinsically available in COMSOL. Therefore, the model was developed by coupling two existing physics (Darcy's law and transport of diluted species in porous media) with the domain ordinary-differential equation. Several mathematical functions were also defined. We consider the 1D analytical solution, developed in a previous study,[33] where the mass transfer coefficient *kc* (eq 17) and dispersion coefficient *De* (eq 18) were assumed to be independent of flow velocity. The domain was also assumed to be homogeneous. Figure 3 shows the initial and boundary conditions used in the simulation model with the analytical solution.

The dimensionless parameters used in the simulations are given in Table 1, where the values of the parameters are fixed

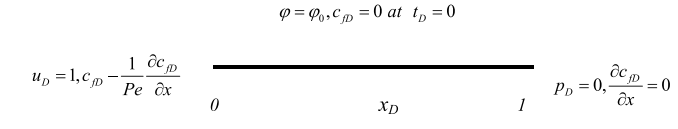

Figure 3. Initial and boundary conditions for the model verification case.

Table 1. Dimensionless Parameters Used in the Simulations

inputs	value	description
b	0.7	constant of the local mass transfer (b)
N_{ac}	0.2	acid capacity number
Sc	2500	Schmidt number
Sh_∞	3	asymptotic Sherwood number
α_{0s}	0.5	tortuosity correction constant
β	2	exponent in structure−property correlation
λ_T	0.1	dispersion transverse coefficient
λ_x	0.5	dispersion longitudinal coefficient
η	$8.00E^{-04}$	pore scale to the Darcy-scale ratio
ϕ^2	20	diffusion Damköhler number

unless otherwise stated. Table 2 summarizes the inputs used in the simulations to replicate the analytical solution. The domain is discretized with fine elements using edge meshing for the 1D case. For the 2D cases, we used a triangular meshing corresponding to about 42,000 mesh elements. Based on previous studies for the 2D problem,[40] simulation results were independent of the mesh size for a degree of freedom that is more than 31,500 mesh elements. In this study, the selected mesh consisted of 42,000 elements. An adaptive time stepping was used in the numerical model, where the solver adjusts the time step to maintain the desired relative tolerance (0.0005). The observed simulation times were the function of the input parameters (mainly Da) and ranged between half an hour to 24 h on a computational workstation.

Figure 4 shows a comparison between the simulation results and the analytical solution, where a good match is obtained between the two solutions. The red curve represents the calculated dissolution front from simulations, while the blue curve represents the analytical solution. The plots on the left show normalized concentration against the normalized distance for different Damköhler numbers. The concentration is normalized by the inlet concentration (C/C_0), and the distance is normalized by the length of the domain (x/L). The normalized concentrations are shown after injecting 42 pore volumes at a convection Damköhler number (Da) of 500. We observe piston-like fronts for dissolution and porosity, which are in excellent agreement with the analytical solution. Figure 4 also shows similar results for a value of the Damköhler number of 10. The dissolution front is sharper for higher values of the Damköhler number.

4.3.2. Numerical Experiments. We conducted simulations for the domain shown in Figure 1, which illustrates the impact of

https://doi.org/10.1021/acsomega.2c05564
ACS Omega 2023, 8, 539−554

Table 2. Physical Parameters Used in the Simulations

input	value − 1D validation case	value − 2D numerical experiment	description
a_0	5000 [1/m]	5000 [1/m]	interfacial area
b	0.7	0.7	constant in local mass transfer
C_0	2.71 [mol/L]	2.71 [mol/L]	inlet concentration of the acid
D_m	4×10^{-10} [m^2/s]	4×10^{-10} [m^2/s]	molecular diffusion coef.
H		2 [cm]	height of the domain
k_0	10 [mD]	5 [mD]	initial permeability
k_s	1.4×10^{-04} [cm/m]	1.4×10^{-04} [cm/m]	surface reaction rate constant
L	15 [cm]	5 [cm]	length of the domain
r_0	1 [μm]	1 [μm]	initial pore radius
Sh_∞	3	3	asymptotic Sherwood number
u_0	0.0016 [cm/s]	varying	injection velocity at the inlet
α_{0s}	0.5	0.5	tortuosity correction constant
α	50 [g/mol]	50 [g/mol]	dissolving power of the acid
β	1	1	pore-broadening parameter
γ	1	1	pore-connectivity parameter
λ_x		0.5	longitudinal dispersion constant
λ_y		0.1	transverse dispersion constant
μ	1 [cP]	1 [cP]	acid viscosity
ρ_s	2.71 [g/cm^3]	2.71 [g/cm^3]	density of carbonate
ν	0.01 [m^2/s]	0.01 [m^2/s]	acid kinematic viscosity
ρ	1000 [kg/m^3]	1000 [kg/m^3]	density of water

different transport and reaction phenomena on carbonate dissolution. The acid is injected from the inlet boundary at a constant rate. The fluid is contained in the domain by applying a no-flux boundary condition in transverse boundaries. A porosity field is randomly disturbed in the domain with an average porosity of 0.2. The numerical implementation of the model is discussed in the previous section. The dimensionless parameters used in the simulations are given in Table 1, and the corresponding physical parameters are given in Table 2. The input data are used as reported in previous studies.[30,31] Figure 5 presents the simulation results for one case at different times for 15% hydrochloric acid injection. The resulting porosity maps are shown at different times, where the velocity vectors, represented by white arrows, depict the wormhole initiation and propagation in the porous medium. Initially, the acid dissolves the face of the rock, and small channels form. The formed channels expand due to the reaction of the acid with the rock. Among these small channels, one channel develops more dominantly, leading the acids to get directed to that dominant channel due to higher conductivity. This is also obvious in the velocity vectors, where all the acid injected flows into the channel. Furthermore, the acid leaks through the wormhole wall causing small branching channels out of the main wormhole. Leakage is mainly caused by diffusion and dispersion. As time progresses, the acid enlarges the width of the channel. Simulations were terminated during acid breakthrough at the outlet.

An important output of the WIPCR models is the time of acid breakthrough (t_{BT}), which is determined as the time at which the pressure drop across the domain decreases by a factor of 100.[33,36] Once the time to breakthrough is known, we calculate the pore volume to breakthrough ($PVTB$) as follows:

$$PVTB = \frac{Q \cdot t_{BT}}{PV} \tag{19}$$

where Q is the acid flow rate, t_{BT} is the breakthrough time, PV is the pore volume of the medium.

The pore volume to breakthrough is an indicator that is used to assess the performance of the acid. A minimum volume of acid is desired to form a maximum length of the wormhole. We monitor the effective permeability across the porous medium over time, which serves as an indicator for $PVTB$. The pressure at the inlet and the velocity at the outlet obtained from the simulation were used to calculate the effective permeability based on Darcy's law. Figure 6 shows the effective permeability (k_{eff}) and the pressure drop across the domain versus time for a test case. The permeability plot can be divided into two parts. Initially, the effective permeability increases at a slow rate, reflecting how the dissolution process progresses before breakthrough, followed by an exponential increase in k_{eff}, resulting from the acid breakthrough. At this stage, the induced wormhole connects the inlet and the outlet of the core. The time at which the wormhole connects the inlet and outlet exhibits a significant reduction in the pressure drop across the domain. This explains the abrupt jump in the effective permeability plot.

Figure 7 illustrates the effect of varying the acid injection rate. The injection rate changes the Peclet number (Pe) and Damköhler number (Da). Low values of the Damköhler number indicate a high injection rate compared to reactivity and vice versa. At a very high injection rate (e.g., Da = 1), no formation of any channels is observed (Figure 7a). However, the porosity in the domain increases. These results highlight the balance between transport and reaction. In this case, the acid residence time is insufficient compared to the reaction time, resulting in partial reactivity of the acid with the carbonate. This dissolution pattern is usually referred to as uniform dissolution. In this scenario, the convection of the acid is more dominant than dispersion. On the other hand, at a very low injection rate (e.g., Da = 30,000), the soaking time of the acid is significant, resulting in complete dissolution (Figure 7f). The acid in this regime produces face dissolution, and dispersion tends to be more dominant than convection, leading to slow propagation of the induced channel. At intermediate injection rates, the acid produces preferential pathways (wormholes) due to the competing effects of convection, dispersion, and reaction. In this regime, the acid only dissolves part of the medium, resulting in fewer volumes of acid required to achieve breakthrough. The behavior of wormhole development and propagation, as Da varies, is shown in Figure 7b−e, where one observes variability in the morphology of the wormholes. For instance, a single wormhole with fewer branches was formed when Da = 500. On the other hand, multiple longer branches were formed from the mother channel when Da = 300, resulting in a ramified dissolution. At higher values of the Damköhler number (Figure 7e), the dissolution channel becomes wider, creating a conical wormhole. This sensitivity study highlights the need to develop an accurate and efficient optimization process for WIPCR.

https://doi.org/10.1021/acsomega.2c05564
ACS Omega 2023, 8, 539−554

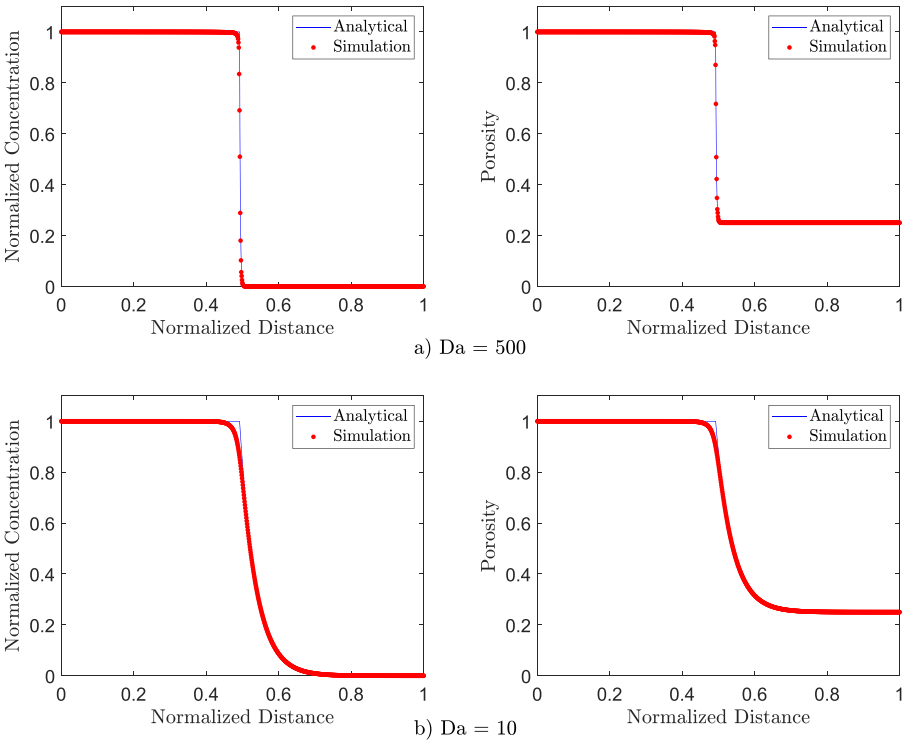

Figure 4. Comparison between analytical and numerical solutions, showing the concentration and porosity distribution after injecting 42 pore volumes of acid, corresponding to Da = 500 in (a) and Da = 10 in (b).

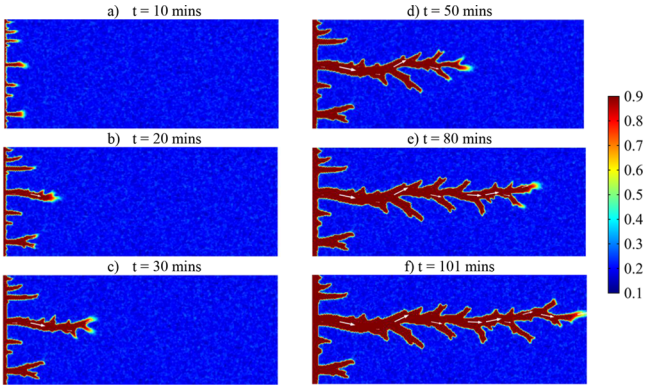

Figure 5. Porosity maps with the velocity vectors (white arrows) showing the solutions until the breakthrough for Da = 500 at different times (a–f) corresponding to 10, 20, 30, 50, 80, and 101 min.

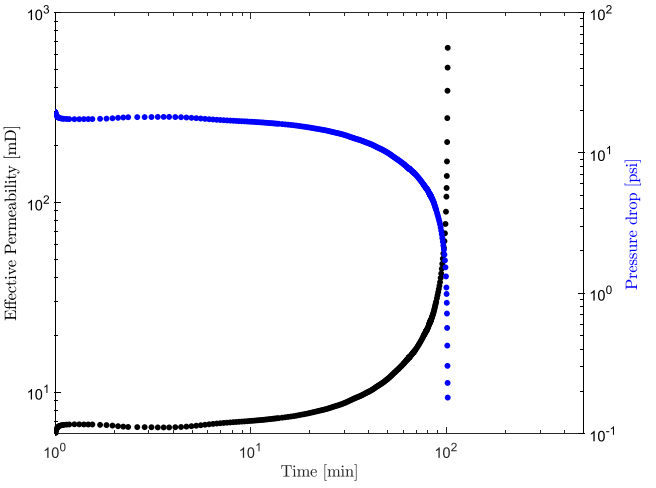

Figure 6. Effective permeability (k_{eff}) across the core as a function of time, which indicates the injected acid breakthrough at the outlet, leading to a conductive channel between the inlet and outlet.

Figure 8 depicts the variation of pore volume to breakthrough ($PVTB$) versus the dimensionless injection rate (reciprocal of the Damköhler number) obtained from the simulations. The simulation input data are presented in Table 2 with varying injection rates. The plot indicates an optimum injection rate to achieve the same length of the dissolution channel with a minimum amount of acid injected. The breakthrough curve provides the general behavior of the experimental observations. For instance, the optimum rate corresponding to the minimum acid usage in Figure 8 is at $Da^{-1} \approx 0.002$, whereas more volume of acid is needed to achieve a breakthrough at lower and higher injection rates. For instance, at low injection rates (e.g., $Da^{-1} = 10^{-4}$), the acid soaking time is long enough to achieve a complete reaction, resulting in the overuse of acid to attain breakthrough. Conversely, as the acid injection rate increases (e.g., $Da^{-1} = 1$), the acid escapes the porous medium with incomplete reactivity, leading to more acid usage to establish channel conductivity between the inlet and outlet.

Figure 9 shows the impact of changing the injection rate on the increase of effective permeability. For example, a lower injection rate requires more time to reach a breakthrough, which can be seen at Da = 1000 compared to other curves. However, as the injection rate increases, the time required for the permeability to increase from the initial mean permeability decreases.

5. RESULTS AND DISCUSSION

5.1. Variable Screening. We address the impact of the variability of input parameters on the model's objective function,

https://doi.org/10.1021/acsomega.2c05564
ACS Omega 2023, 8, 539−554

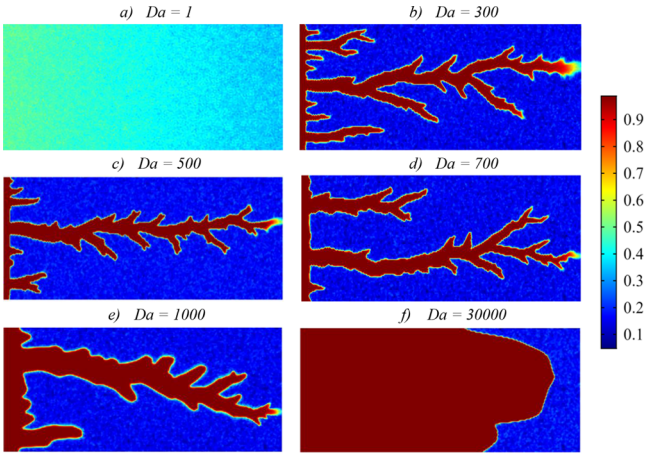

Figure 7. Porosity maps at different values of the convection Damköhler number corresponding to *Da* = (a) 1, (b) 300, (c) 500, (d) 700, (e) 1000, and (f) 30,000, indicating different behaviors of the stimulation process as a result of the competing mechanisms of convection, diffusion, and reaction.

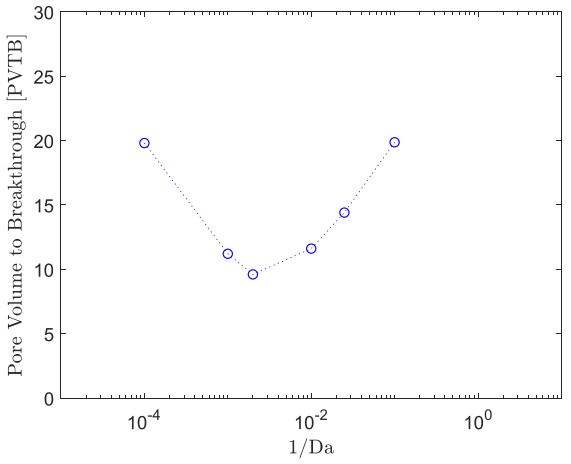

Figure 8. Pore volume to breakthrough versus the reciprocal of *Da*, showing the optimum injection conditions (minimum *PVTB*) to achieve a fast breakthrough with low acid usage.

corresponding to the pore volume to breakthrough (*PVTB*) and the effective permeability (k_{eff}) of the medium. We use the DoE to identify the significant factors affecting the model's response. We implement folded Placket–Burman DoE to determine the significant variables in the simulation model. We monitor the acid concentration at the outlet to serve as an indicator for the simulation stopping criteria, corresponding to channel breakthrough and the end of the stimulation job. This approach was found to be more robust than using pressure drop or effective permeability as stopping criteria. Figure 9 confirms the robustness of the selected stopping criterion for all tested cases, which is verified by the consistency of the final effective permeability of the system. The time to breakthrough is defined as the time at which 10% of the inlet acid concentration reaches the outlet of the core. This criterion does not impact the final outcome. Table 3 summarizes the range of the uncertain parameters used in the DoE, corresponding to the surface reaction rate, diffusion coefficient, initial pore radius, and interfacial surface reported in the literature.[65−67] We performed the analysis with dimensionless numbers instead of the physical parameters.

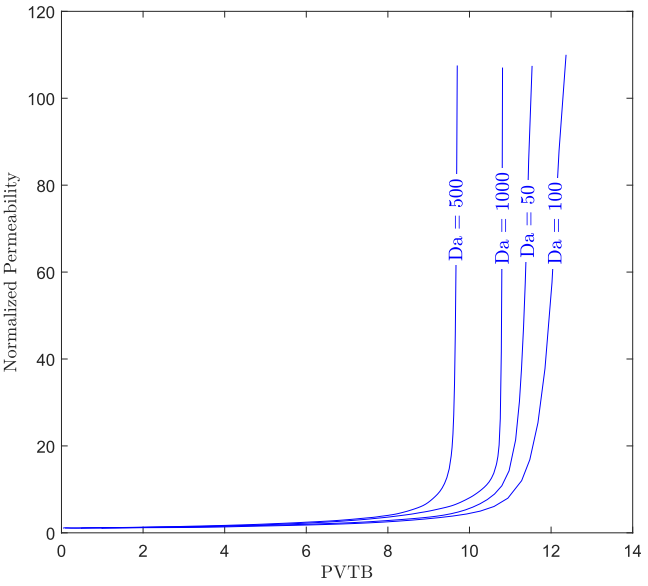

Figure 9. Influence of varying the injection rate (dimensionless convection Damköhler number) on the effective permeability of the porous medium established by acid stimulation.

Table 3. Range of Variability for the Uncertainty Parameters Used in the DoE

inputs	range	description
b	[0.1−0.7]	constant of the local mass transfer (b)
Da	[50−1000]	convection Damköhler number
N_{ac}	[0.01−0.2]	acid capacity number
Pe	[200−20,000]	Peclet number
Sc	[250−2500]	Schmidt number
Sh_{∞}	[2−4.36]	asymptotic Sherwood number
α_{0s}	[0.1−0.5]	tortuosity correction constant
β	[1−2]	exponent in the structure−property correlation
η	[4.00E^{-05}−8.00E^{-04}]	pore-scale to Darcy-scale ratio
λ_T	[0.1−0.5]	dispersion transverse coefficient
λ_x	[0.1−0.5]	dispersion longitudinal coefficient
ϕ_0	[0.05−0.2]	initial mean porosity
ϕ^2	[0.07−20]	diffusion Damköhler number

We conducted 33 simulations to identify the significant variables using Plackett–Burman's DoE. The results obtained from the simulation are used to build a nonlinear regression model. We then utilize the regression model to calculate the effect of each variable on the objective function. Figure 10a shows the Pareto chart for the standardized effect on *PVTB*. The acid capacity number is the most significant parameter. This dimensionless number represents the stoichiometry of the reaction. It is defined as the volume of carbonate that can be dissolved in a unit volume of the acid. The second significant parameter is the initial mean porosity, which is essential to calculate pore-scale parameters such as the initial pore radius and interfacial surface area. This finding is consistent with the analytical solution proposed in a previous study[30] given by

$$PVTB = \frac{(1 - \phi_0)}{N_{ac}\phi_0} \tag{20}$$

The above equation is a simple correlation to estimate *PVTB* as a function of porosity and the acid capacity number. The last parameter that appears to be significant is the pore-connectivity

https://doi.org/10.1021/acsomega.2c05564
ACS Omega 2023, 8, 539−554

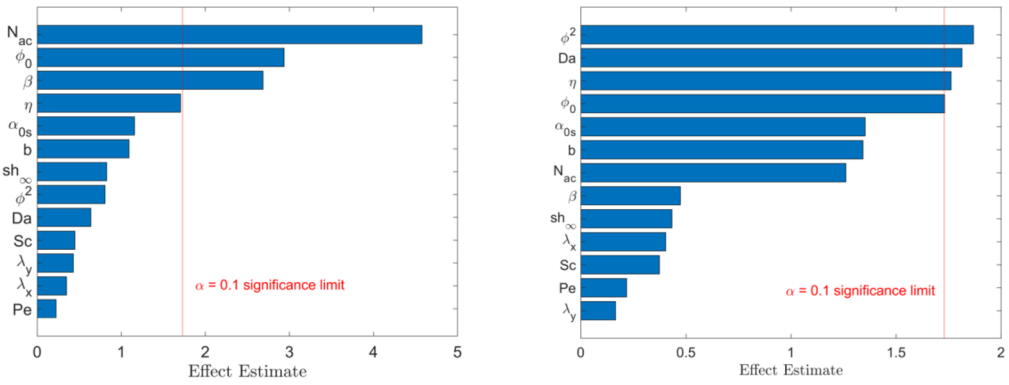

a) Parameter ranking relative to *PVTB* b) Parameter ranking relative to k_{eff}

Figure 10. Pareto plot for the standardized effect on *PVTB* (a), and k_{eff} (b), showing the ranking of the significant parameters.

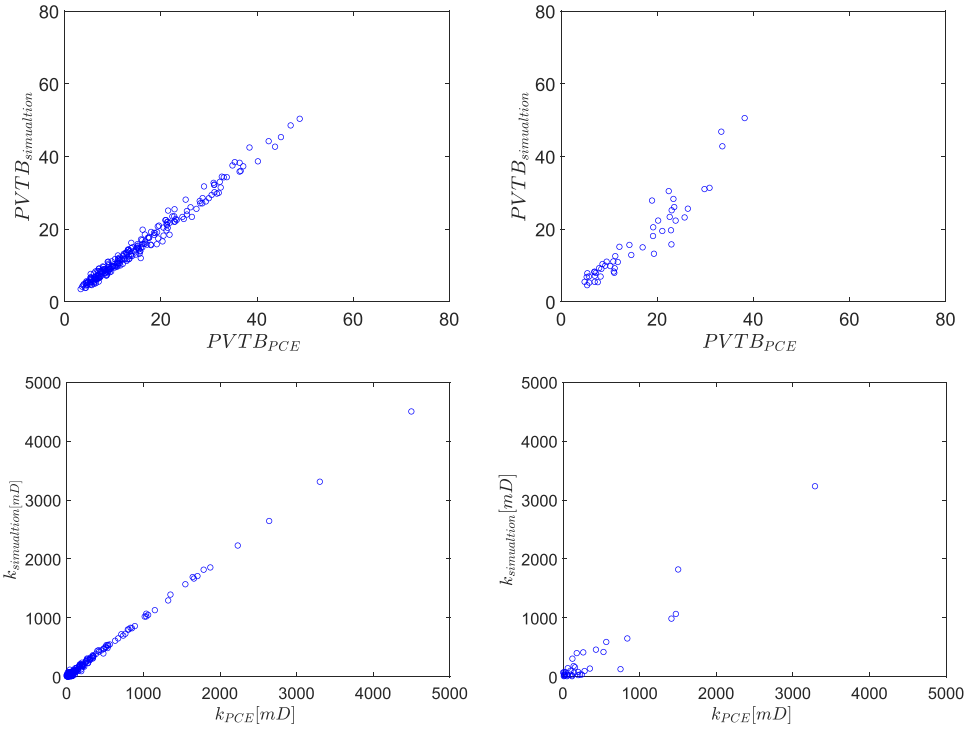

Figure 11. Comparisons between the simulation results and PCE for the *PVTB* and the effective permeability. On the left side, 250 samples were used in the experimental design, and on the right side, 50 samples were used for verification.

parameter (β). The aforementioned parameters are statistically significant at the significant limit of 0.1, while the remaining ones are less significant based on their prior interval of uncertainties.

Figure 10b shows the Pareto chart for the standardized effect on effective permeability. The effective permeability is related to the pressure drop across the rock. During dissolution, the pressure drop decreases as the acid reacts with the rock mineral, creating a conductive path for fluid flow. This explains why the diffusion Damköhler number (ϕ^2) and the convection Damköhler number (Da) top the list as the most significant factors impacting the effective permeability. Also, the pore-scale to Darcy-scale ratio and the initial mean porosity appears to be significant. The initial mean porosity is used to update the rock's permeability, which explains the strong dependency of permeability on the initial mean porosity. The aforementioned parameters are statistically significant on the effective permeability at the significant limit of 0.1. The remaining parameters are statistically insignificant. Based on the screening step, we select six parameters to conduct further analysis, including the diffusion Damköhler number (ϕ^2), the convection Damköhler number (Da), the initial mean porosity (ϕ_0), the pore scale to Darcy scale ratio (η), the acid capacity number (N_{ac}), and the pore-connectivity parameter (β).

5.2. Development of the Surrogate Model. Polynomial chaos expansions (PCEs) were constructed and trained to replace the finite-element model in the evaluation of GSA and optimization. Therefore, the reliability of the study depends on the accuracy of the PCEs, which require careful verification. To do so, we consider the previous 2D problem with properties, as presented in Table 1, corresponding to six variables. The identified insignificant parameters are kept constant at their most likely values, as listed in Table 1. The six input parameters are assumed to be uniformly distributed over the ranges of variability. The surrogate model (PCEs) is constructed using a

https://doi.org/10.1021/acsomega.2c05564
ACS Omega 2023, 8, 539−554

DoE consisting of 300 samples, based on a quasi-random sampling technique to cover the parameters' space. The workflow was developed using UQLAB software.[68] Several PCE models were constructed to capture multiple outputs of the simulations, including pore volume to breakthrough ($PVTB$), effective permeability (k_{eff}), as well as the 2D spatial distribution of acid concentration in the domain at the breakthrough time.

In the case of acid distribution, component-wise PCE was constructed for each node in the simulation domain. Out of the 300 simulations from the DoE, 250 experiments were used to construct the PCEs, and 50 were kept to validate the model. We use the adaptive basis strategy in UQLAB to optimize the order of the constructed PDE, which was tested within the range of 1 to 6. The optimization process of the PCE order minimizes the leave-one-out (ε_{LOO}) cross-validation error, which checks the predictability of PCE on sets of data that were not part of the training. Figure 11 represents parity plots that compare the results from the surrogate and simulation models for input parameters corresponding to the data sets used to build the proxy and validation sets that are not utilized to construct the PCE. We notice a good match for training and a reasonable match for validation. This accuracy of PCE, corresponding to leave-one-out (ε_{LOO}) cross-validation error within 1.68%, was found to be good enough to perform GSA and Monte Carlo simulations.

Figure 12 shows a comparison between the results from the simulation model and values obtained from the component-wise

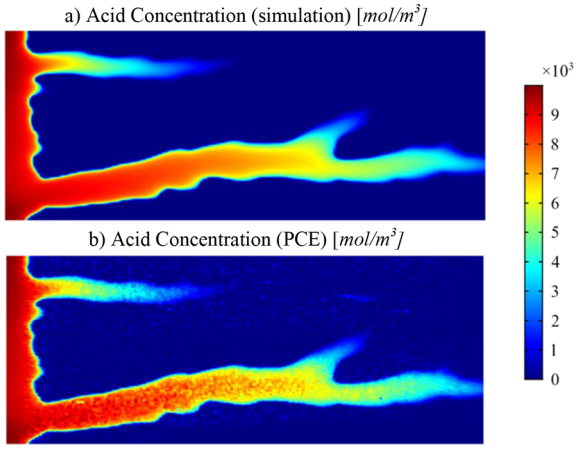

Figure 12. Comparison between the values of (a) the simulation results of the acid concentration map and (b) the concentration distribution obtained from the multivariate PCE built on simulation nodes at the breakthrough time.

PCE for the 2D acid concentration distribution at the breakthrough time. Given the complexity of the flow and transport processes in the heterogeneous domain, the PCE-predicted concentration map is in excellent agreement with finite-element simulation. It should be noted that the component-wise PCE allows calculating the Sobol sensitivity indices map in the domain, as demonstrated in the next section.

5.3. Uncertainty Propagation Analysis. Postprocessing of the PCE coefficients allows calculating the total Sobol indices (SIs) that are utilized to perform uncertainty propagation analysis. Furthermore, we can assess the impact of the input factors on the model response by calculating the marginal effect. This process is useful to extend the surrogate model for new samples. Hence, we can calculate the univariate effect by evaluating the variability of the model's response (i.e., pore volume to breakthrough and effective permeability) to a specific parameter using the surrogate model. This is achieved by varying the factor of interest and keeping other parameters constant at their average values. Figure 13 shows the results of GSA for the spatial distribution of the acid concentration by varies for the identified significant parameters. Figure 13a represents the mean distribution of the acid concentration calculated from the PCE moments at the breakthrough time. The mean value of the acid concentration is calculated at each node of the simulation domain. It uses the coefficient (y_0) with the constant basis ($\Phi_0 = 1$). Because of the complexity of the problem, the mean acid concentration does not fully capture the model's response. In each experiment, the wormhole initiates and propagates from a different point on the core. This is because of the interplay between the reaction and transport.

By varying the input parameters, such as initial mean porosity, initial pore radius, and the interfacial surface area available for reaction, wormholes may initiate from different points and propagate through different pathways. The mean value of the acid concentration obtained from the surrogate model captures the general behavior of the dissolution. Dissolution of the rock face occurs at the inlet of the core, and later, a channel develops. Figure 13b shows the standard deviation of acid concentration, illustrating the deviation of concentration from its mean in the 2D domain. The high variance of the acid concentration corresponds to where dissolution occurs the most. It can be interpreted by the acid leaking into the wormhole wall because of diffusion and dispersion, which creates this high variability around the region where dissolution occurs. We assess the sensitivity of the spatial acid concentration to the uncertain input parameters with the total Sobol indices (SIs). Figure 13c shows the total SIs of the initial mean porosity. One observes that the uncertainty of this parameter has an insignificant impact on acid concentration where dissolution occurs. Figure 13d shows the total SIs for the acid capacity number.

The acid concentration is highly sensitive to this parameter's uncertainty where the SIs are high in the active dissolution regions. Surrounding the dissolution channels, the SIs are lower due to the leak-off to the channel walls by diffusion and dispersion. At the center of the channel, the SI has high values, corresponding to the dominance of convection, making the acid concentration sensitive to the acid capacity number. It is important to emphasize that the total SI considers the overall contribution of a particular parameter to the model's response, including interactions and nonlinear effects. Hence, it allows for the ranking of the input parameters according to their significance to the output of interest. This shows that the acid capacity number (N_{ac}) (Figure 13d) is the most significant parameter compared to other input parameters. In this case, the total SI is more prominent in the dissolution region, where the variance of the acid concentration is maximum. The acid concertation is not sensitive to initial mean porosity (Figure 13c), as the region where the SI is high corresponds to negligible variance. Figure 14 shows examples from the 300 experiments on how the wormhole initiates and propagates differently in each case, showing different apertures of the wormholes.

Figure 15 presents the sensitivity of the model's responses (i.e., $PVTB$ and k_{eff}) to the uncertain parameters that we considered in this study. The figure shows the bar plot of the total sensitivity indices corresponding to the uncertain input parameters. These sensitivity indices, along with the univariate effect, are used to understand the uncertainty of the output of

https://doi.org/10.1021/acsomega.2c05564
ACS Omega 2023, 8, 539−554

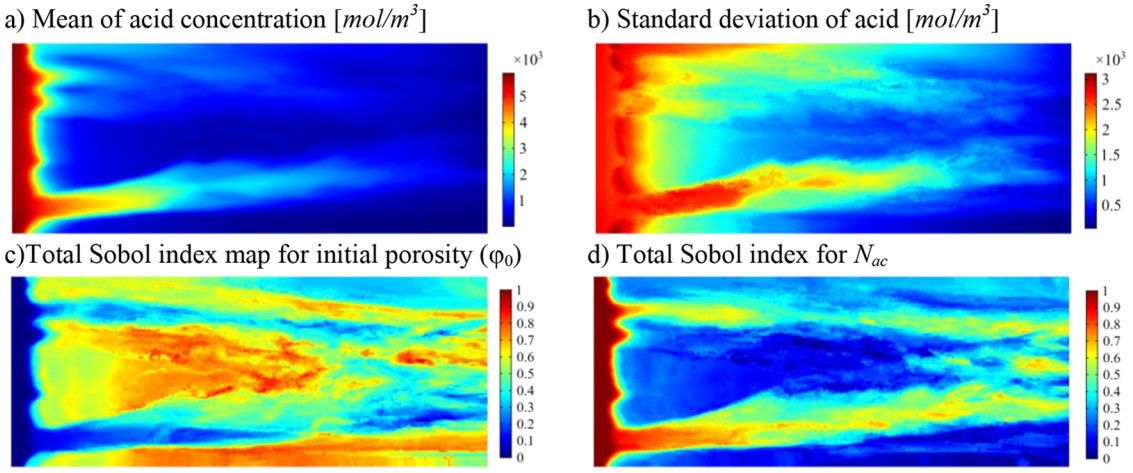

Figure 13. GSA results for the 2D spatial distribution of the acid concentration, where (a) mean of the acid concentration [mol/m^3], (b) standard deviation of the acid concentration [mol/m^3], (c) total Sobol indices map for initial mean porosity, and (d) total Sobol indices map for the acid capacity number (N_{ac}).

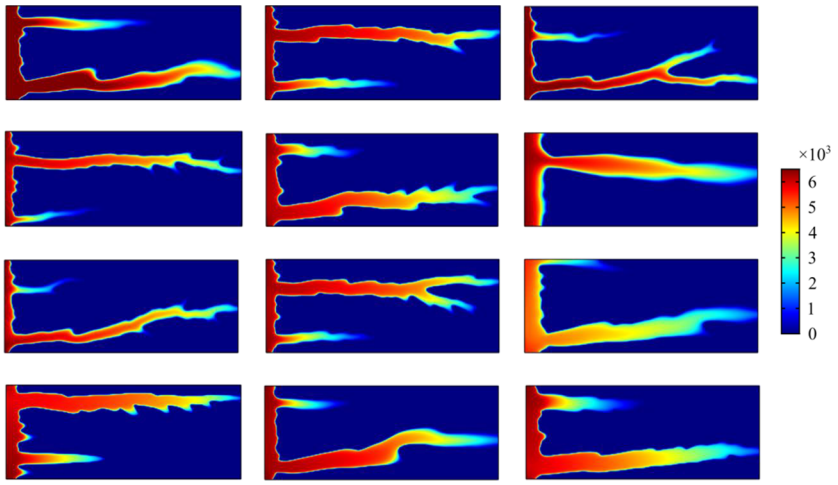

Figure 14. Spatial distribution of acid concentration [mol/m^3] from the simulation results at the final simulation time, illustrating how the wormhole initiates and propagates in different cases from DoE.

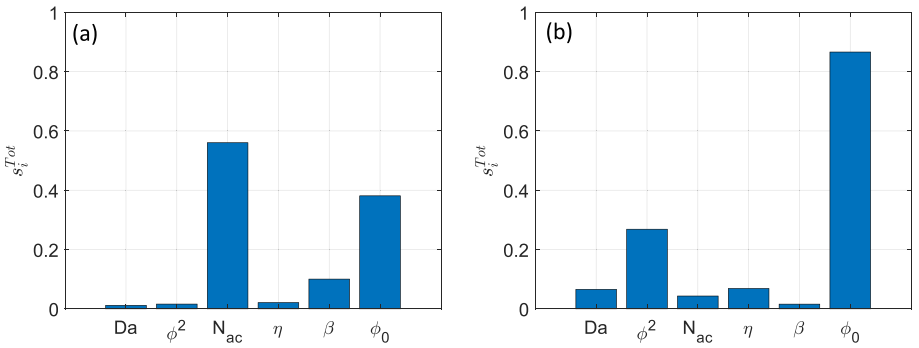

Figure 15. Total SIs for (a) *PVTB* and (b) effective permeability (k_{eff}).

the reactive transport model related to incomplete knowledge of the input parameters. Figure 15a indicates that the highest contribution to the *PVTB* is due to the acid capacity number, initial mean porosity, and the broadening exponent, while Figure 15b shows that the initial mean porosity and diffusion Damköhler number (ϕ^2) are main influential parameters for the effective permeability.

The acid capacity number (N_{ac}) is the most significant parameter, with a total SI of 0.59. The univariate effect of N_{ac} and ϕ_0 on *PVTB* is presented in Figure 16a,b, respectively. The acid capacity number is mainly a function of the acid's inlet concentration. Figure 16a shows that the *PVTB* decreases with the increase in the acid capacity number (N_{ac}), which is in agreement with previous studies.[30,59] As the acid concentration increases, the volume of acid required decreases. We also notice

https://doi.org/10.1021/acsomega.2c05564
ACS Omega 2023, 8, 539−554

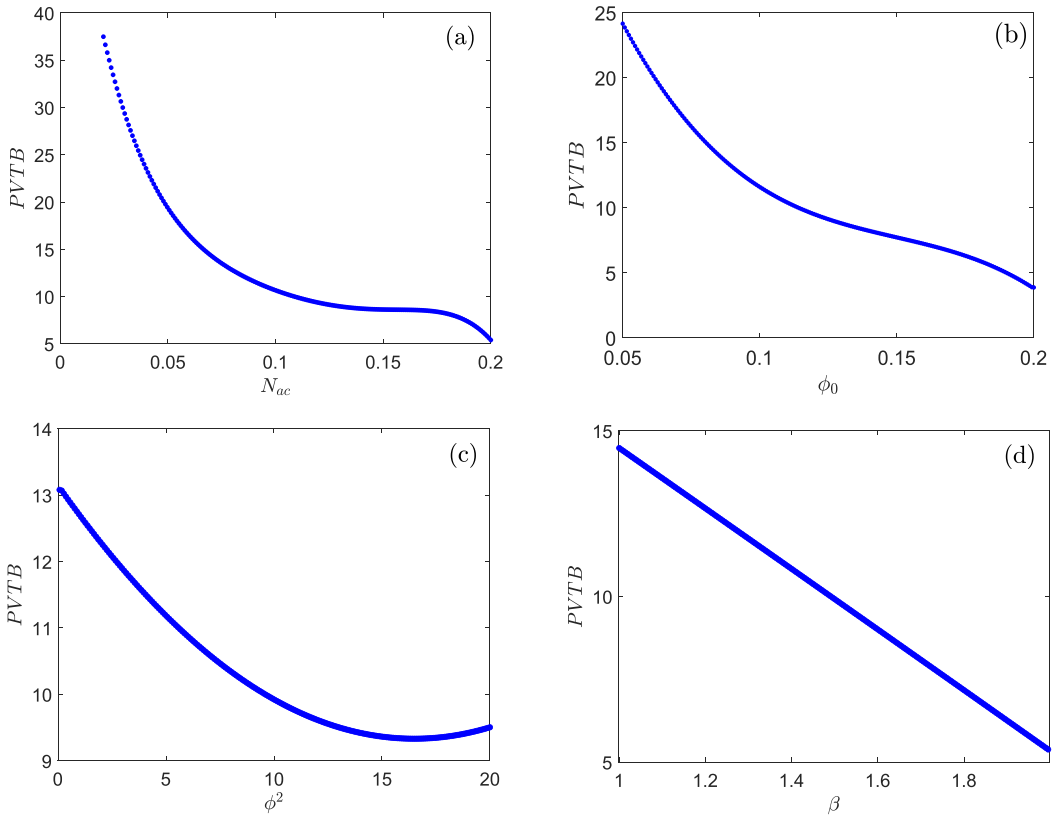

Figure 16. Univariate effect of the input parameters (a) N_{ac}, (b) ϕ_0, (c) ϕ^2, and (d) β on the *PVTB*.

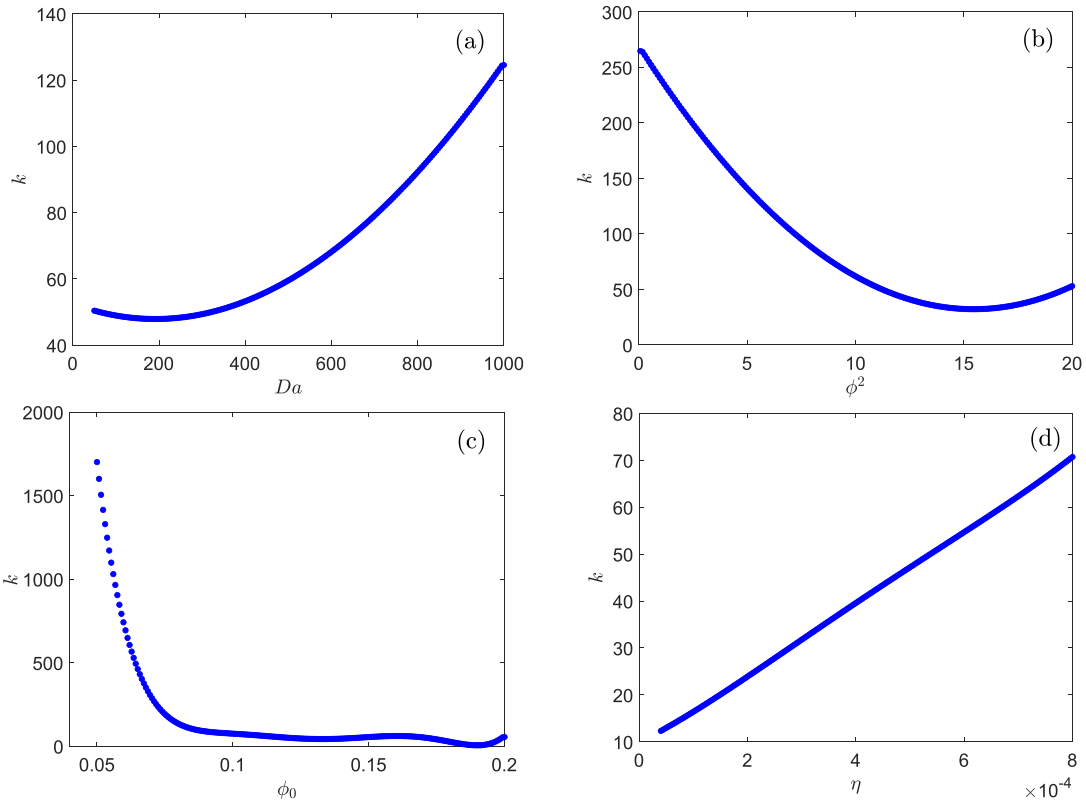

Figure 17. Univariate effect of the input parameters (a) k, (b) ϕ^2, (c) ϕ_0, and (d) η on the effective permeability.

that when the acid capacity number is greater than 0.1 (15% HCL), its effect on pore volume to breakthrough is less significant. Figure 16b shows that *PVTB* decreases with an increase in the mean porosity, which is coherent with previous results.[31,34] The presence of more minerals can explain this in the low-porosity rocks compared to the high-porosity rocks.

https://doi.org/10.1021/acsomega.2c05564
ACS Omega 2023, 8, 539−554

Hence, more acid is required to dissolve the rock mineral in rock with low mean porosity. Figure 16d shows that *PVTB* decreases with an increase in the pore-broadening parameter. The increase in this exponent causes the wormhole diameter to be smaller, which explains why less volume of acid is required. Figure 16c shows the univariate effect of the diffusion Damköhler number (ϕ^2). *PVTB* decreases with an increase in the diffusion Damköhler number until the value of $\phi^2 \approx 10$. At this point, the effect is not pronounced. In fact, this is a transition between reaction regimes from the kinetically controlled regime to the mass transfer regime.[30] Figure 15b shows that most of the contribution to the effective permeability (k_{eff}) is due to initial mean porosity and the diffusion Damköhler number. The initial mean porosity (φ_0) is the most influential parameter with a total SI of 0.84. This is evident from the univariate effect in Figure 17c. We notice that the effective permeability decreases with the increase in porosity. We need to highlight here that this effective permeability corresponds to the permeability at breakthrough. Rocks have complicated structures, especially at the pore scale. For small porosity, the increase in the permeability is higher to achieve acid breakthrough, which might explain the behavior of the plot.

Figure 1b shows the variability of the effective permeability with respect to ϕ^2. The effective permeability decreases with the increase in ϕ^2. Also, a similar behavior is observed in the transition between the kinetically controlled regimes to the mass transfer regime. Figure 1a shows that as *Da* increases, the effective permeability increases. This can be attributed to the influence of convective transport and reaction. A wider channel is observed at high *Da*, causing less pressure drop and eventually higher permeability. Figure 17d shows the relationship between the final effective permeability and η. There is a proportional relationship between the two variables. An increase in η increases the pore radius, which explains this relationship.

6. CONCLUSIONS

This study provides an integrated framework to model carbonate acidizing with uncertainty propagation and GSA that combines continuum-based modeling, variable screening, and variance decomposition techniques. The main conclusions are

- The model estimates the optimum injection rate of the used chemical where the pore volume to breakthrough is minimized while maximizing the increase in effective permeability of the rock formation.
- The diffusion Damköhler number, convection Damköhler number, initial mean porosity, pore scale to the Darcy scale ratio, acid capacity number, and the pore-connectivity parameter are found to be the significant parameters.
- The Sobol sensitivity map shows that the distribution of the acid concentration is sensitive to the acid capacity number, especially in the region where dissolution occurs.
- The variability of the pore volume to breakthrough is mainly impacted by the acid capacity number. The second main significant factor is the initial mean porosity, followed by the pore-broadening parameter.
- Understanding the uncertainty parameters in the reactive transport model is critical to optimize the process. Furthermore, it is important to minimize the volume requirement as acid is often prepared from fresh water, which has environmental concerns.
- Potential future work includes understanding the acidizing process in a layered system with sorted distribution of reservoir properties. The modeling should be performed at the wellbore-reservoir scale, where the thermal effect is also considered.

APPENDIX A. GOVERNING EQUATIONS WITH DIMENSIONLESS VARIABLES

The governing equations can then be written in the dimensionless form as follows:

$$(u_D, v_D) = \left(-\kappa_D \frac{\partial p_D}{\partial x_D}, -\kappa_D \frac{\partial p_D}{\partial y_D}\right) \tag{A1}$$

$$\frac{\partial \varphi}{\partial t_D} + \nabla \cdot \mathbf{u}_D = 0 \tag{A2}$$

$$\frac{\partial(\varphi c_{fD})}{\partial t_D} + \nabla \cdot (\mathbf{u}_D c_{fD}) = -\frac{DaA_{vD} c_{fD}}{1 + \frac{\phi^2 r_D}{Sh}} + \nabla \cdot (\mathbf{D}_{eD} \cdot \nabla c_{fD}) \tag{A3}$$

$$D_{eD,X} = \alpha_{os} \varphi Pe + \lambda_x |\mathbf{u}_D| r_D \eta,\ D_{eD,T} = \alpha_{os} \varphi Pe + \lambda_T |\mathbf{u}_D| r_D \eta \tag{A4}$$

$$\frac{\partial(\varphi)}{\partial t_D} = -\frac{DaN_{ac}A_{vD}}{1 + \frac{\phi^2 r_D}{Sh}} c_{fD} \tag{A5}$$

$$Sh = Sh_\infty + bRe_p^{1/2} Sc^{1/3} \tag{A6}$$

$$Re_p = \frac{\eta Pe}{Sc} |\mathbf{u}_D| r_D \tag{A7}$$

Then, the initial and boundary conditions can then be written as follows:

$$C_{fD} - \varphi D_{eD,x} \frac{\partial C_{fD}}{\partial x_D} = 1, \quad x = 0 \tag{A8}$$

$$-\frac{\kappa_{xD}}{\mu} \frac{\partial p_D}{\partial x_D} = 1, \quad \frac{\partial p_D}{\partial y_D} = 0, \quad x = 0 \tag{A9}$$

$$n \cdot \nabla p_D = 0,\ n \cdot \nabla C_{fD} = 0, \text{ transverse boundries} \tag{A10}$$

$$p_D = 0, \quad \frac{\partial C_{fD}}{\partial x_D} = 0, \quad x = 1 \tag{A11}$$

$$\varphi = \varphi_0 + \hat{f},\ C_{fD} = 0 \quad \text{at } t_D = 0, \text{ where } \hat{f} \in \{-\Delta\varphi_0, \Delta\varphi_0\} \tag{A12}$$

APPENDIX B. SOBOL INDICES

Sobol sensitivity analysis helps us understand how the uncertainty propagates in the used reactive transport model. Consider the response of the mathematical model[56,57] to be $Y = M(X)$, where this model depends on several uncertainty parameters, $X = \{X_1, X_2, ..., X_M\}$. The response of the system can be decomposed as follows:

https://doi.org/10.1021/acsomega.2c05564
ACS Omega 2023, 8, 539−554

$$Y = M(\mathbf{X}) = M_0 + \sum_{i=1}^{M} M_i(X_i) + \sum_{1\le i<j\le M} M_{ij}(X_i, X_j) + \cdots + M_{1,2,\ldots,M}(X_1, \ldots, X_M) \quad \text{(B1)}$$

Here, M_0 is a constant that is equal to the expected value of $M(X)$, a condition must hold for the decomposition such that its integral over its independent input variables is zero, that is:

$$\int_{\Gamma_{X_{ik}}} M_{i_1,i_2,\ldots,i_s}(X_{i2}, X_{i2}, \ldots, X_{i2}) f_{X_{ik}}(X_{ik}) = 0, \quad (1 \le k \le s) \quad \text{(B2)}$$

where $\Gamma_{X_{ik}}$ and $f_{X_{ik}}(X_{ik})$ represent the support of X_{ik}, and the marginal probability density function, respectively. The orthogonality and uniqueness of M_i lead to the following variance compositions:

$$D = \mathrm{Var}[M(X)] = \sum_{u\neq 0} D_u = \sum_{u\neq 0} \mathrm{Var}[M_u(X_u)] \quad \text{(B3)}$$

where $u = \{i_1, i_2,\ldots,i_m\} \subseteq \{1, 2,\ldots,M\}$ represents the index sets, and X_u are the subvectors in u. Here, D_u represents the partial variance, defined by

$$D_u = \mathrm{Var}[M_u(X_u)] = E[M_u^2(X_u)] \quad \text{(B4)}$$

Thus, the Sobol sensitivity indices are expressed as

$$S_u = \frac{D_u}{D} \quad \text{(B5)}$$

The total Sobol sensitivity indices that include the contribution of an input parameter with the effect of the rest of the parameters are defined as follows:

$$S_i^{\mathrm{T}} = \sum_{\vartheta_i} \frac{D_u}{D}, \ (\vartheta_i = \{u \supset i\}) \quad \text{(B6)}$$

The sensitivity indices can be calculated in many ways. The traditional method is through Monte Carlo simulations. To reduce computations, we utilized polynomial chaos expansion[54] for the calculation of these indices. Each output that is used to assess the efficiency of a system is written into a set of multivariate polynomials, as follows:

$$Y = M(X) \approx \sum_{\alpha\in A} y_\alpha \Phi_\alpha(X) \quad \text{(B7)}$$

where A is a set of chosen multi-index $\alpha = \{\alpha_1, \alpha_2,\ldots, \alpha_2\}$ which identifies the multivariate polynomial components $(\Phi_\alpha(X))$, and y_α is the corresponding polynomial coefficient.

Various methods can evaluate the corresponding polynomial coefficients for given basis functions. The common strategy used to compute the coefficients is the projection and the regression method. The regression method is performed based on minimizing an objective function that represents the difference in predictions between simulations and the surrogate model, PCE. Once PCE is built, the total variance (D) and mean value $(\hat{\mu})$ of the model response can be evaluated as follows:

$$\hat{\mu} = y_0, \quad D = \sum_{\alpha\in A\setminus 0} y_\alpha^2 \quad \text{(B8)}$$

Using the PCE coefficients, the total SIs can be expressed as follows:

$$S_i^{\mathrm{T}} = \sum_{\alpha\in A_i^{\mathrm{T}}\setminus 0} y_\alpha^2/D, \quad (A_i^{\mathrm{T}} = \{\alpha \in A: \alpha_i > 0\}) \quad \text{(B9)}$$

The marginal effects[69] can also be calculated from PCE, which provides the relation between the model's response and the sensitive input parameters. The marginal effect can be evaluated as follows:

$$E[M(X)|X_i = x_i] = M_0 + \sum_{\alpha\in A_i} y_\alpha \Phi_\alpha(x_i) \quad \text{(B10)}$$

AUTHOR INFORMATION

Corresponding Author

Hussein Hoteit − *Physical Science and Engineering Division, King Abdullah University of Science and Technology (KAUST), Thuwal 23955, Saudi Arabia;* orcid.org/0000-0002-3900-7272; Email: Hussein.hoteit@kaust.edu.sa

Authors

Qasim Sahu − *Physical Science and Engineering Division, King Abdullah University of Science and Technology (KAUST), Thuwal 23955, Saudi Arabia;* Present Address: Saudi Aramco Co., Dhahran, Saudi Arabia (Q.S.)

Marwan Fahs − *Institut Terre et Environnement de Strasbourg, University of Strasbourg, CNRS, ENGEES, Strasbourg 67084, France*

Complete contact information is available at: https://pubs.acs.org/10.1021/acsomega.2c05564

Author Contributions

The manuscript was written through the contributions of all authors. All authors have given approval for the final version of the manuscript.

Notes

The authors declare no competing financial interest.

ACKNOWLEDGMENTS

The authors thank the supporting institution, King Abdullah University of Science and Technology, University of Strasbourg, and Saudi Aramco.

REFERENCES

(1) Kargarpour, M. A. Carbonate Reservoir Characterization: An Integrated Approach. *J. Pet. Explor. Prod. Technol.* **2020**, *10*, 2655−2667.

(2) Schön, J. H.*Physical Properties of Rocks: Fundamentals and Principles of Petrophysics*; Elsevier, 2015.

(3) Akbar, M.; Vissapragada, B.; Alghamdi, A. H.; Allen, D.; Herron, M.; Carnegie, A.; Dutta, D.; Olesen, J.-R.; Chourasiya, R. D.; Logan, D. A Snapshot of Carbonate Reservoir Evaluation. *Oilfield Rev.* **2000**, *12*, 20−41.

(4) Ahmed, M.; Habbtar, A.; Al-Malki, B.; Rahim, Z.; Al-Anazi, H.; Al-Kanaan, A.; El-Mofty, W.; Bukovac, T. First Application of Limited Entry Multistage Matrix Acidizing in Saudi Arabia's Deep Gas Development Program − A Case Study for Improved Acid Stimulation and Placement Techniques. *Soc. Pet. Eng − SPE Saudi Arabia Sect. Tech. Symp. Exhib.* **2013**, *2013*, 428−435.

(5) Economides, M. J.; Nolte, K. G.*Reservoir Stimulation*; Prentice Hall: Englewood Cliffs, NJ, 1989; Vol. 2.

(6) Panjalizadeh, H.; Safari, A. R.; Kamani, M. An Efficient Interpretation Method for Matrix Acidizing Evaluation and Optimization in Long Heterogeneous Carbonate Reservoirs. *SPE Prod. Oper.* **2021**, *36*, 780−794.

(7) Wang, Y.; Hill, A. D.; Schechter, R. S.The Optimum Injection Rate for Matrix Acidizing of Carbonate Formations. In *SPE Annual Technical Conference and Exhibition*; Society of Petroleum Engineers, 1993.
(8) Fredd, C. N.; Fogler, H. S.Alternative Stimulation Fluids and Their Impact on Carbonate Acidizing. In *SPE Formation Damage Control Symposium*; OnePetro, 1996.
(9) Huang, T.; Ostensen, L.; Hill, A. D.Carbonate Matrix Acidizing with Acetic Acid. In *SPE international symposium on formation damage control*; Society of Petroleum Engineers, 2000.
(10) Nasr-El-Din, H. A.; Solares, J. R.; Al-Mutairi, S. H.; Mahoney, M. D.Field Application of Emulsified Acid-Based System to Stimulate Deep, Sour Gas Reservoirs in Saudi Arabia. In *SPE Annual Technical Conference and Exhibition*; Society of Petroleum Engineers, 2001.
(11) Al-Khaldi, M. H.; Nasr-El-Din, H. A.; Blauch, M. E.; Funkhouser, G. P. New Findings on Damage Potential, Geochemical Reaction Mechanisms, and Production Enhancement Applications for Citric Acid. *SPE J.* **2005**, *10*, 267−275.
(12) Mahmoud, M.; Saleh Aljawad, M.; Shahzad Kamal, M.; Ali, A.; Al-Nakhli, A. Two-Stage Stimulation of Gas Carbonate Reservoirs with High Anhydrite Content: Experimental and Modeling Study. *Energy Fuels* **2020**, *34*, 9978−9989.
(13) Li, H.; Shi, Y. Study on the Performance Degradation of Sandstone under Acidification. *ACS Omega* **2020**, *5*, 28333−28340.
(14) Qi, N.; Li, B.; Chen, G.; Fang, M.; Li, X.; Liang, C. Optimum Fluid Injection Rate in Carbonate Acidizing Based on Acid Dissolution Morphology Analysis. *Energy Fuels* **2017**, *31*, 13448−13453.
(15) Tariq, Z.; Aljawad, M. S.; Hassan, A.; Mahmoud, M.; Al-Ramadhan, A. Chelating Agents as Acid-Fracturing Fluids: Experimental and Modeling Studies. *Energy Fuels* **2021**, *35*, 2602−2618.
(16) Barri, A.; Hassan, A.; Mahmoud, M. Carbonate Stimulation Using Chelating Agents: Improving the Treatment Performance by Optimizing the Fluid Properties. *ACS Omega* **2022**, *7*, 8938−8949.
(17) Bazin, B. From Matrix Acidizing to Acid Fracturing: A Laboratory Evaluation of Acid/Rock Interactions. *SPE Prod. Facil.* **2001**, *16*, 22−29.
(18) Izgec, O.; Keys, R. S.; Zhu, D.; Hill, A. D.An Integrated Theoretical and Experimental Study on the Effects of Multiscale Heterogeneities in Matrix Acidizing of Carbonates. In *SPE Annual Technical Conference and Exhibition*; Society of Petroleum Engineers, 2008.
(19) Yoo, H.; Kim, Y.; Lee, W.; Lee, J. An Experimental Study on Acid-Rock Reaction Kinetics Using Dolomite in Carbonate Acidizing. *J. Pet. Sci. Eng.* **2018**, *168*, 478−494.
(20) Qiu, X.; Aidagulov, G.; Ghommem, M.; Edelman, E.; Brady, D.; Abbad, M. Towards a Better Understanding of Wormhole Propagation in Carbonate Rocks: Linear vs. Radial Acid Injection. *J. Pet. Sci. Eng.* **2018**, *171*, 570−583.
(21) Sayed, M.; Cairns, A. J.; Sahu, Q.Low Viscosity Acid Platform: Benchmark Study Reveals Superior Reaction Kinetics at Reservoir Conditions. In *International Petroleum Technology Conference 2020*; IPTC 2020, 2020.
(22) Wu, Y.; Salama, A.; Sun, S. Parallel Simulation of Wormhole Propagation with the Darcy−Brinkman−Forchheimer Framework. *Comput. Geotech.* **2015**, *69*, 564−577.
(23) Liu, P.; Yao, J.; Couples, G. D.; Ma, J.; Iliev, O. 3-D Modelling and Experimental Comparison of Reactive Flow in Carbonates under Radial Flow Conditions. *Sci. Rep.* **2017**, *7*, 17711.
(24) Akanni, O. O.; Nasr-El-Din, H. A.The Accuracy of Carbonate Matrix-Acidizing Models in Predicting Optimum Injection and Wormhole Propagation Rates. In *SPE Middle East Oil and Gas Show and Conference, MEOS, Proceedings*, 2015; Vol. 2015-January, pp 618−635.
(25) Hung, K. M.; Hill, A. D.; Sepehrnoori, K. A Mechanistic Model of Wormhole Growth in Carbonate Matrix Acidizing and Acid Fracturing. *J. Pet. Technol.* **1989**, *41*, 59−66.
(26) Algive, L.; Bekri, S.; Vizika, O. Pore-Network Modeling Dedicated to the Determination of the Petrophysical-Property Changes in the Presence of Reactive Fluid. *SPE J.* **2010**, *15*, 618−633.
(27) Tansey, J.; Balhoff, M. T. Pore Network Modeling of Reactive Transport and Dissolution in Porous Media. *Transp. Porous Media* **2016**, *113*, 303−327.
(28) Liu, M.; Mostaghimi, P. Characterisation of Reactive Transport in Pore-Scale Correlated Porous Media. *Chem. Eng. Sci.* **2017**, *173*, 121−130.
(29) Liu, M.; Shabaninejad, M.; Mostaghimi, P. Predictions of Permeability, Surface Area and Average Dissolution Rate during Reactive Transport in Multi-Mineral Rocks. *J. Pet. Sci. Eng.* **2018**, *170*, 130−138.
(30) Panga, M. K. R.; Ziauddin, M.; Balakotaiah, V. Two-Scale Continuum Model for Simulation of Wormholes in Carbonate Acidization. *AIChE J.* **2005**, *51*, 3231−3248.
(31) Jia, C.; Huang, Z.; Sepehrnoori, K.; Yao, J. Modification of Two-Scale Continuum Model and Numerical Studies for Carbonate Matrix Acidizing. *J. Pet. Sci. Eng.* **2021**, *197*, No. 107972.
(32) Hassan, A.; Saleh Aljawad, M.; Mahmoud, M. An Artificial Intelligence-Based Model for Performance Prediction of Acid Fracturing in Naturally Fractured Reservoirs. *ACS Omega* **2021**, *6*, 13654−13670.
(33) Maheshwari, P.; Ratnakar, R. R.; Kalia, N.; Balakotaiah, V. 3-D Simulation and Analysis of Reactive Dissolution and Wormhole Formation in Carbonate Rocks. *Chem. Eng. Sci.* **2013**, *90*, 258−274.
(34) Kalia, N.; Balakotaiah, V. Effect of Medium Heterogeneities on Reactive Dissolution of Carbonates. *Chem. Eng. Sci.* **2009**, *64*, 376−390.
(35) Kalia, N.; Balakotaiah, V. Modeling and Analysis of Wormhole Formation in Reactive Dissolution of Carbonate Rocks. *Chem. Eng. Sci.* **2007**, *62*, 919−928.
(36) Ghommem, M.; Zhao, W.; Dyer, S.; Qiu, X.; Brady, D. Carbonate Acidizing: Modeling, Analysis, and Characterization of Wormhole Formation and Propagation. *J. Pet. Sci. Eng.* **2015**, *131*, 18−33.
(37) Liu, P.; Yan, X.; Yao, J.; Sun, S. Modeling and Analysis of the Acidizing Process in Carbonate Rocks Using a Two-Phase Thermal-Hydrologic-Chemical Coupled Model. *Chem. Eng. Sci.* **2019**, *207*, 215−234.
(38) Wang, L.; Mou, J.; Mo, S.; Zhao, B.; Liu, Z.; Tian, X. Modeling Matrix Acidizing in Naturally Fractured Carbonate Reservoirs. *J. Pet. Sci. Eng.* **2020**, *186*, No. 106685.
(39) Qi, N.; Chen, G.; Liang, C.; Guo, T.; Liu, G.; Zhang, K. Numerical Simulation and Analysis of the Influence of Fracture Geometry on Wormhole Propagation in Carbonate Reservoirs. *Chem. Eng. Sci.* **2019**, *198*, 124−143.
(40) Mahmoodi, A.; Javadi, A.; Sola, B. S. Porous Media Acidizing Simulation: New Two-Phase Two-Scale Continuum Modeling Approach. *J. Pet. Sci. Eng.* **2018**, *166*, 679−692.
(41) Jia, C.; Sepehrnoori, K.; Huang, Z.; Zhang, H.; Yao, J. Numerical Studies and Analysis on Reactive Flow in Carbonate Matrix Acidizing. *J. Pet. Sci. Eng.* **2021**, *201*, No. 108487.
(42) Oladyshkin, S.; Class, H.; Helmig, R.; Nowak, W. A Concept for Data-Driven Uncertainty Quantification and Its Application to Carbon Dioxide Storage in Geological Formations. *Adv. Water Resour.* **2011**, *34*, 1508−1518.
(43) Camacho, A.; Talavera, A.; Emerick, A. A.; Pacheco, M. A. C.; Zanni, J. Uncertainty Quantification in Reservoir Simulation Models with Polynomial Chaos Expansions: Smolyak Quadrature and Regression Method Approach. *J. Pet. Sci. Eng.* **2017**, *153*, 203−211.
(44) Santoso, R.; Hoteit, H.; Vahrenkamp, V.Optimization of Energy Recovery from Geothermal Reservoirs Undergoing Re-Injection: Conceptual Application in Saudi Arabia. In *SPE Middle East Oil and Gas Show and Conference, MEOS, Proceedings*; Society of Petroleum Engineers (SPE), 2019; Vol. 2019-March.
(45) Su, T. R.; Huang, T. H.; Kao, C. T.; Ng, H. Y.; Chiu, Y. C.; Hsu, T. T. The Calcium Channel Affect Osteogenic Differentiation of Mesenchymal Stem Cells on Strontium-Substituted Calcium Silicate/Poly-ε-Caprolactone Scaffold. *Processes* **2020**, *8*, 197.
(46) Clavijo, S. P.; Addassi, M.; Finkbeiner, T.; Hoteit, H. A Coupled Phase-Field and Reactive-Transport Framework for Fracture Propagation in Poroelastic Media. *Sci. Rep.* **2022**, *12*, 17819.

https://doi.org/10.1021/acsomega.2c05564
ACS Omega 2023, 8, 539−554

(47) Oelkers, E. H.; Arkadakskiy, S.; Afifi, A. M.; Hoteit, H.; Richards, M.; Fedorik, J.; Delaunay, A.; Torres, J. E.; Ahmed, Z. T.; Kunnummal, N.; Gislason, S. R. The Subsurface Carbonation Potential of Basaltic Rocks from the Jizan Region of Southwest Saudi Arabia. *Int. J. Greenhouse Gas Control* **2022**, *120*, No. 103772.
(48) Rajabi, M. M.; Fahs, M.; Panjehfouladgaran, A.; Ataie-Ashtiani, B.; Simmons, C. T.; Belfort, B. Uncertainty Quantification and Global Sensitivity Analysis of Double-Diffusive Natural Convection in a Porous Enclosure. *Int. J. Heat Mass Transfer* **2020**, *162*, No. 120291.
(49) Fajraoui, N.; Fahs, M.; Younes, A.; Sudret, B. Analyzing Natural Convection in Porous Enclosure with Polynomial Chaos Expansions: Effect of Thermal Dispersion, Anisotropic Permeability and Heterogeneity. *Int. J. Heat Mass Transfer* **2017**, *115*, 205−224.
(50) Hoteit, H.; Addassi, M.Integrated Uncertainty Quantification for Reactive Transport Modeling of CO2 Mineralization in Basalts. In *3rd EAGE Geochemistry Workshop*; European Association of Geoscientists & Engineers, 2021; Vol. *2021*, pp 1−5.
(51) Yang, X.; Shao, Q.; Hoteit, H.; Carrera, J.; Younes, A.; Fahs, M. Three-Dimensional Natural Convection, Mixing and Entropy Generation in Heterogeneous Porous Medium. *Adv. Water Resour.* **2021**, *155*, No. 103992.
(52) Benetatos, C.; Giglio, G. Coping with Uncertainties through an Automated Workflow for 3D Reservoir Modelling of Carbonate Reservoirs. *Geosci. Front.* **2021**, *12*, 100913.
(53) Sobol, I. M. Global Sensitivity Indices for Nonlinear Mathematical Models and Their Monte Carlo Estimates. *Math. Comput. Simul.* **2001**, *55*, 271−280.
(54) Sudret, B.Global Sensitivity Analysis Using Polynomial Chaos Expansions. In *Reliability Engineering and System Safety*; Elsevier, 2008; pp 964−979.
(55) Santoso, R.; Torrealba, V.; Hoteit, H. Investigation of an Improved Polymer Flooding Scheme by Compositionally-Tuned Slugs. *Processes* **2020**, *8*, 197.
(56) Safari, M.; Gholami, R.; Jami, M.; Ananthan, M. A.; Rahimi, A.; Khur, W. S. Developing a Porosity-Permeability Relationship for Ellipsoidal Grains: A Correction Shape Factor for Kozeny-Carman's Equation. *J. Pet. Sci. Eng.* **2021**, *205*, No. 108896.
(57) Balakotaiah, V.; West, D. H. Shape Normalization and Analysis of the Mass Transfer Controlled Regime in Catalytic Monoliths. *Chem. Eng. Sci.* **2002**, *57*, 1269−1286.
(58) Gupta, N.; Balakotaiah, V. Heat and Mass Transfer Coefficients in Catalytic Monoliths. *Chem. Eng. Sci.* **2001**, *56*, 4771−4786.
(59) Jia, C.; Sepehrnoori, K.; Huang, Z.; Yao, J. Modeling and Analysis of Carbonate Matrix Acidizing Using a New Two-Scale Continuum Model. *SPE J.* **2021**, *26*, 2570−2599.
(60) Ghanem, R.; Owhadi, H.; Higdon, D.*Handbook of Uncertainty Quantification*; 2017; pp 1 −2053.
(61) He, X.; Zhu, W.; AlSinan, M.; Kwak, H.; Hoteit, H.CO2 Storage Capacity Prediction In Deep Saline Aquifers: Uncertainty and Global Sensitivity Analysis. In *Day 2 Tue, February 22, 2022*; IPTC, 2022.
(62) Guo, L.; Fahs, M.; Hoteit, H.; Gao, R.; Shao, Q. Uncertainty Analysis of Seepage-Induced Consolidation in a Fractured Porous Medium. *Comput. Model. Eng. Sci.* **2021**, *129*, 279−297.
(63) Sun, H.; Chawathé, A.; Hoteit, H.; Shi, X.; Li, L. Understanding Shale Gas Flow Behavior Using Numerical Simulation. *SPE J.* **2015**, *20*, 142−154.
(64) Adepoju, O. O.; Hussein, H.; Chawathe, A.Assessment of Chemical Performance Uncertainty in Chemical EOR Simulations. In *Society of Petroleum Engineers −- SPE Reservoir Simulation Conference 2017*; Society of Petroleum Engineers, 2017; pp 127−140.
(65) Arvidson, R. S.; Ertan, I. E.; Amonette, J. E.; Luttge, A. Variation in Calcite Dissolution Rates: A Fundamental Problem? *Geochim. Cosmochim. Acta* **2003**, *67*, 1623−1634.
(66) Lai, P.; Moulton, K.; Krevor, S. Pore-Scale Heterogeneity in the Mineral Distribution and Reactive Surface Area of Porous Rocks. *Chem. Geol.* **2015**, *411*, 260−273.
(67) Mohammadi, M.; Shadizadeh, S. R.; Manshad, A. K.; Mohammadi, A. H. Experimental Study of the Relationship between Porosity and Surface Area of Carbonate Reservoir Rocks. *J. Pet. Explor. Prod. Technol.* **2020**, *10*, 1817−1834.
(68) Stefano, M.; Bruno, S.UQLab: A Framework for Uncertainty Quantification in Matlab. In *Vulnerability, Uncertainty, and Risk*, 2021; pp 2554−2563.
(69) Deman, G.; Konakli, K.; Sudret, B.; Kerrou, J.; Perrochet, P.; Benabderrahmane, H. Using Sparse Polynomial Chaos Expansions for the Global Sensitivity Analysis of Groundwater Lifetime Expectancy in a Multi-Layered Hydrogeological Model. *Reliab. Eng. Syst. Saf.* **2016**, *147*, 156−169.

https://doi.org/10.1021/acsomega.2c05564
ACS Omega 2023, 8, 539−554